Negligible effect of brain MRI data preprocessing for tumor segmentation.

Ekaterina Kondrateva[b,a,*], Polina Druzhinina[b,a,*], Alexandra Dalechina[c],
Svetlana Zolotova[c], Andrey Golanov[c], Boris Shirokikh[b,a], Mikhail Belyaev[b,a],
Anvar Kurmukov[a,*]

[a]*Artificial Intelligence Research Institute (AIRI), Moscow, Russia*
[b]*Skolkovo Institute of Science and Technology, Moscow, Russia*
[c]*National Medical Research Center for Neurosurgery, Moscow Gamma Knife Center,
Moscow, Russia*

Abstract

Magnetic resonance imaging (MRI) data is heterogeneous due to differences in device manufacturers, scanning protocols, and inter-subject variability. A conventional way to mitigate MR image heterogeneity is to apply preprocessing transformations such as anatomy alignment, voxel resampling, signal intensity equalization, image denoising, and localization of regions of interest. Although a preprocessing pipeline standardizes image appearance, its influence on the quality of image segmentation and on other downstream tasks in deep neural networks has never been rigorously studied.

Experiments on three publicly available datasets evaluate the effect of different preprocessing steps in intra- and inter-dataset training scenarios. Results demonstrate that most popular standardization steps add no value to network performance; moreover, preprocessing can hamper performance. Our results suggest that image intensity normalization approaches do not contribute to model accuracy because of the reduction of signal variance with image standardization. Additionally, the contribution of skull-stripping in data preprocessing is almost negligible if measured in terms of estimated tumor volume.

The only essential transformation for accurate deep learning analysis is the unification of voxel spacing across the dataset. In contrast, inter-subjects anatomy alignment in the form of non-rigid atlas registration is not necessary and intensity equalization steps (denoising, bias-field correction and histogram matching) do not improve performance.

The study code is accessible online[1].

Keywords: Brain MRI, segmentation, preprocessing, nnU-net, UNETR, SAM

---

[*]Authors contributed equally
[1]https://github.com/MedImAIR/brain-mri-processing-pipeline

1. Introduction

In recent years, modern deep neural networks (DNN) have steadily improved the quality of automatic segmentation pipelines in medical imaging. Specifically, for the task of brain tumor segmentation, the performance of DNNs has achieved human-level efficiency Chang et al. [2019]. This advancement can be explained by the improvement of DNN architectures and the growth of the training datasets. For example, the size of the BraTS competition Bakas et al. [2018] training dataset increased from 100 subjects in 2013 to 2000 subjects in 2021. Simultaneously, top-performing algorithms have progressed from random forest and gradient boosting trees on radiomics features: first to fully convolutional networks, then to u-shaped UNet and UNet-like networks, and finally to Vision transformers.

In contrast, the preprocessing steps used to prepare data for analysis seem to have undergone considerably fewer changes. For instance, the set of preprocessing steps for brain MRI images has remained relatively stable and has been reproduced across the majority of papers on the topic from the early 2010s until now. Here we challenge the conventional pipelines for MRI image processing and question their necessity for accurate prediction with regard to new advanced deep learning machinery.

The traditional brain MRI preparation steps could be divided into four distinct categories:

- The first category is subject-wise image alignment, typically in the form of rigid registration of one MRI sequence to another, (e.g. T2-FLAIR onto T1 with contrast enhancement). This step is mandatory if one uses multiple MR modalities to predict a single segmentation map to ensure correct alignment between ground truth annotation and corresponding image's voxels.

- The second category is voxels resampling to some standard. The most common methods are voxel resampling to homogeneous spacing (often $1 \times 1 \times 1$ mm^3) and non-rigid registration to some anatomical atlas.

- The third category includes steps that affect voxels' intensity distribution, such as bias-field correction (such as N4 correction Tustison et al. [2010]), intensity normalization (typically in a form of image-wise z-scoring), image denoising methods (e.g. SUSAN Smith and Brady [1997]), and histogram equalization Nyúl et al. [2000].

- Finally, the last step that is preserved in almost all the papers is skull stripping as a method to localize regions of interest (the brain tissue), implement feature selection to ease localization, and reduce the amount of False Positives Chang et al. [2019].

While the motivation behind applying these steps is clearly to standardize image appearance and remove different sources of domain shift Kondrateva et al. [2021], these steps are computationally costly and their utility for deep-learning

2

segmentation lacks investigation. Specifically, it is widely known that increasing variability of the data by data augmentation (image resizing, non linear intensity transformations, applying noise, etc.) leads to improved DNN performance Wightman et al. [2021]. However, data preprocessing works quite in the opposite way by reducing data variance.

In this study we analyze the most popular preprocessing steps for brain MRIs and measure their influence on deep-learning based tumor segmentation tasks. We analyze different preprocessing strategies and recommend the minimal pipeline required for accurate segmentation with the benefits of lower computational costs and improved reproducibility.

2. Related works

Image preprocessing is a de-facto standard first step in almost all deep learning pipelines for medical image analysis Nixon and Aguado [2019]. In this domain, data preparation is convenient due to two major causes:

- diversity in scanning protocols and therefore diverse spatial resolutions and image intensity profiles Kurmukov et al. [2021],

- large image sizes and small sample sizes, thus leading to high-dimension learning compounding negative effects on model generalisability Berisha et al. [2021].

For example, a typical multi-institutional brain MRI dataset consists of images with varying resolutions and acquisition parameters (depending on scanning protocol). Therefore, a majority of studies utilize data preprocessing pipelines. We select several recent publications on brain MRI segmentation to identify the most common preprocessing steps (see Table 1).

Table 1: Common preprocessing steps for multi-modal brain MRI image analysis. Checkmarks represent the step mentioned in the study and x-marks are placed if the step is missing or unclear.

Preprocessing step	Resample to image size	Resample to spacing	Atlas registration	Bias-field correction	Denoising	Histogram matching	Skull stripping
Győrfi et al. [2021]	✓	✓	✓	✓	✗	✓	✓
Ranjbarzadeh et al. [2021]	✓	✓	✓	✗	✗	✗	✓
Pei et al. [2020]	✓	✓	✓	✓	✓	✓	✓
Menze et al. [2021]	✗	✓	✗	✗	✗	✗	✓
Ermiş et al. [2020]	✓	✗	✗	✗	✗	✗	✓
Eijgelaar et al. [2020]	✓	✓	✓	✓	✗	✗	✓
Rathore et al. [2017]	✓	✓	✓	✓	✓	✓	✓
Wang et al. [2019]	✗	✗	✗	✗	✗	✗	✗
Bakas et al. [2018]	✗	✗	✓	✗	✗	✗	✓
Kickingereder et al. [2019]	✗	✗	✗	✗	✗	✗	✓
Bakas et al. [2022]	✗	✗	✓	✗	✗	✗	✓

The overall brain MRI data preprocessing pipeline can be divided into four groups of methods.

2.1. Intra-subject alignment (rigid registration)

During this step different MR sequences from a single patient are reoriented in a similar way and rigidly registered. This step is applied in all studies that analyze multi-sequence MRI Győrfi et al. [2021]; Ranjbarzadeh et al. [2021]; Pei et al. [2020]; Menze et al. [2021]; Ermiş et al. [2020]; Eijgelaar et al. [2020].

2.2. Inter-subject alignment

This step standardizes the size of images across the dataset. Most of the observed papers use voxel resampling to an isotropic voxel (e.g. $1 \times 1 \times 1$ mm^3), or to the same image resolution (in voxels, e.g. $256 \times 256 \times 256$), or both, by means of non-rigid atlas registration Győrfi et al. [2021]; Ranjbarzadeh et al. [2021]; Pei et al. [2020]; Menze et al. [2021] and Ermiş et al. [2020]; Eijgelaar et al. [2020]; Rathore et al. [2017]; Bakas et al. [2018]. The only exceptions are two studies that analyze the data acquired with a unified scanning protocol (isotropic voxel) Kickingereder et al. [2019]; Wang et al. [2019].

2.3. Non-linear intensity correction and enhancement

Multi-institutional studies typically use some intensity or noise correction approaches, with the most popular being histogram matching Győrfi et al. [2021]; Pei et al. [2020]; Rathore et al. [2017], bias-field correction Győrfi et al. [2021]; Pei et al. [2020]; Eijgelaar et al. [2020]; Rathore et al. [2017], and denoising Pei et al. [2020]; Rathore et al. [2017].

Histogram equalization (harmonization or matching) methods standardize images by aligning their intensity distributions Nyúl et al. [2000]. Denoising algorithms filter the image whilst preserving the underlying structure Smith and Brady [1997]. Finally, bias-field correction methods mitigate the effects of magnetic field variation Tustison et al. [2010], see Figure 2.

Most of the observed studies apply z-scoring Ranjbarzadeh et al. [2021]; Pei et al. [2020]; Menze et al. [2021]; Ermiş et al. [2020]; Rathore et al. [2017]; Wang et al. [2019]; Kickingereder et al. [2019] prior to analysis. This is a common data normalization approach for all computer vision algorithms Patro and Sahu [2015] and is not specific to medical imaging.

2.4. Skull stripping

Finally, all but one of the observed papers Wang et al. [2019] use skull stripping, arguing that non-brain tissue is a significant source of error for downstream tumor segmentation Chang et al. [2019]. Authors point out that skull stripping reduces the number of False Positives and improves segmentation quality.

2.5. Novelty of the proposed study

In general, researchers experimenting on single-institutional data or data collected under unified acquisition protocol tend to use fewer preprocessing steps. On the contrary, the analysis of heterogeneous multi-center data typically includes a data preparation pipeline. For example, the data preparation pipeline

for the most-known benchmark dataset for multi-institutional brain MRI segmentation[2] includes image reorientation, altas registration Rohlfing et al. [2010], bias-field correction, and skull stripping Thakur et al. [2020].

These MRI preprocessing methods have been exploited by scientists for several decades. Yet to date there is no consensus regarding which of the methods should be applied for deep-learning-based analysis. In the present work we demonstrate that the effect of most standardization steps is negligible even for relatively small data collection.

To the best of our knowledge, there have been two similar attempts to analyze the influence of preprocessing steps for medical imaging tasks. Authors of Moradmand et al. [2020] test how preprocessing influences radiomics features calculation (for brain MRI), and de Raad et al. [2021] investigate the influence of data augmentation for three medical imaging tasks (brain and knee MRI and liver CT segmentation).

2.6. Contributions

In our study we focus on preprocessing steps used primarily for brain MRI. Our contribution is three-fold. First, we numerically estimate the effect of 7 common preprocessing steps: resizing images to equal size,inter-subject atlas registration,resampling voxels to equal size, bias-field correction, image denoising, histogram matching, skull stripping; with state-of-the-art deep learning architectures that are both convolutional and attention-based. This effect is assessed in two scenarios: training from scratch and fine-tuning from a larger dataset.

Second, we propose an explanation for the observed low (or even negative) influence of image intensity correction techniques on model accuracy. For that we compare segmented tissue with the rest of the brain before and after preprocessing.

Third, we suggest a minimal preprocessing pipeline for multi-sequence, multi-protocol brain MRI segmentation studies, consisting of two steps[3]:

1. voxel resampling (to roughly align images across the dataset),
2. skull stripping.

The last step results in a marginal but statistically significant improvement in terms of segmentation quality, especially for smaller (< 100 subjects) datasets, though it could be omitted for larger datasets with little drop in accuracy.

3. Methods

In the current study we test how different preprocessing pipelines affect the quality of a downstream deep learning segmentation model. We compare

---

[2]https://cbica.github.io/CaPTk/preprocessing_brats.html

[3]We assume intra-subject sequence alignment and z-scoring to be mandatory first and last preprocessing steps, respectively.
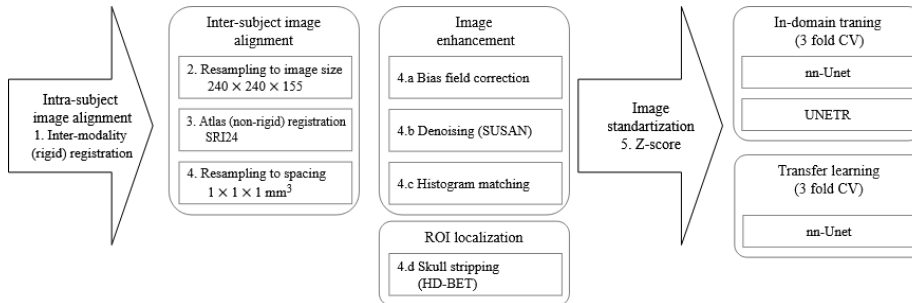
Figure 1: Study experimental pipeline. Steps in arrows are mandatory, steps in blocks are optional. Steps 4.a-d are performed after step 4. The minimal preprocessing pipeline consists of steps 1 and 5. Thus, we have 8 different preprocessing pipelines in total.

eight preprocessing pipelines using two segmentation models (convolutional and attention based), Figure 1. Additionally, we test if the optimal preprocessing pipeline changes in a transfer learning scenario (vs training from scratch) by fine-tuning a model pretrained on a different dataset (with the same preprocessing).

In the following sections we provide information on experimental design and a detailed description of the preprocessing steps, neural network setups, quality metrics, and datasets.

3.1. Experimental design

We compare preprocessing pipelines (Figure 1) in two scenarios:

1. Training a segmentation model from scratch.
2. Fine-tuning a segmentation model from a related or a similar task.

Thus, we check if different preprocessing pipelines result in better in-domain training, and an improved fine-tuning/knowledge transfer in a cross-dataset regime. In the second scenario we only consider whole model fine-tuning as it is the most common approach to knowledge transfer Wang et al. [2021]; Dai et al. [2019].

3.2. Preprocessing steps

In all experiemnts we use multi-sequence datasets consisting of 4 MRI sequences: T1 weighted (T1), T1 weighted with contrast enhancement (CT1), T2 weighted (T2), and T2-FLAIR (FLAIR). We start each preprocessing pipeline with rigid registration (rotation, shift and linear interpolation of voxel size) of every MR sequence to CT1 or FLAIR (depending on the dataset) independently for each subject. This step aligns different MR sequences (from the same subject) with each other and the existing tumour annotation. After that, we proceed with preprocessing steps as described in Figure 1. We end each preprocessing pipeline with image-wise Z-scoring:

$$X_s = \frac{X - \mathrm{mean}(X)}{\mathrm{std}(X)}.$$

6

3.2.1. Inter-subject alignment

After the intra-subject rigid registration, we apply one of three methods to align images across the dataset (inter-subject):

- resizing images to the same size $240 \times 240 \times 155$ voxels;

- resampling to an isotropic voxels' size $1 \times 1 \times 1$ mm^3;

- a non-rigid atlas registration to SRI24 atlas Rohlfing et al. [2010].

The latter results in both of the same images of size $240 \times 240 \times 155$, and an isotropic voxel $1 \times 1 \times 1$ mm^3. All transformations were performed by ANTs utilities Avants et al. [2009].

3.2.2. Image enhancement

The next step is applying one of three algorithms of image intensity correction:

- bias-field correction,

- denoising,
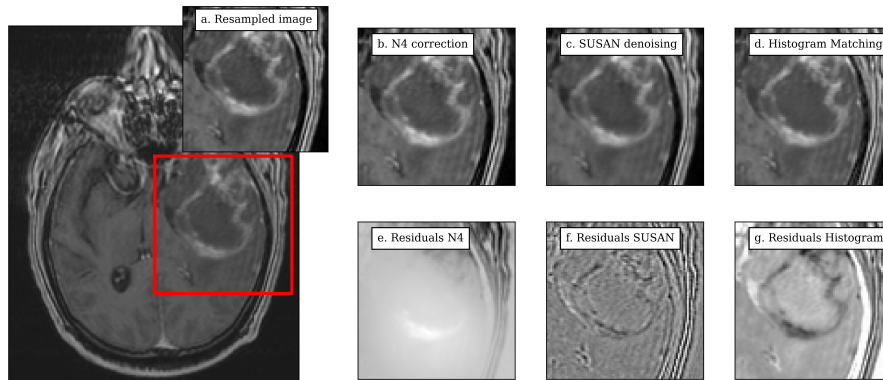
- histogram standardization.

Figure 2: Visualization of three methods of image intensity correction used in the ablations study. The top raw (b-d) showing the image segment with tumor after preprocessing of (a) an example CT1 MR image from GBM data after resampling to [1,1,1] voxel size; (b) N4 correction of the image; (c) SUSAN denoising of the image; (d) Histogram standartization to GBM sample; The bottom row (e-g) showing image residuals as voxelwise difference between the original resampled image and the preprocessed one.

Bias-field is a smooth, non-heterogeneous and low-frequency signal which corrupts MRI images. It is generally believed that algorithms which postprocess MRI images such as segmentation or classification do not produce satisfactory results without correcting for the bias field signal Juntu et al. [2005]. To test the

impact of such a correction we use a popular N4 algorithm Tustison et al. [2010], implemented in Simple-ITK Beare et al. [2018] as a containerized solution from the CaPTk toolbox.

SUSAN is a method of nonlinear image smoothing and denoising Smith and Brady [1997] that, while old, is still used nowadays for noise reduction. We use an FSL implementation of SUSAN. These two steps were applied for each MR image individually.

Finally, to homogenize grayvalue distribution across images in the dataset, we apply a histogram equalization Nyúl et al. [2000], as implemented in TorchIO library Pérez-García et al. [2021]. To estimate the parameters of histogram matching we use training folds, and the same transformation is applied to the data from test folds. Histogram matching is applied sequence-wise, meaning that we equalize voxels' histograms for each MR sequence separately Li et al. [2021].

These steps are applied after resampling images to an isotropic voxel (step 4, Figure 1). As we show in the results, there is no statistical differences between steps 2-4. We thus use voxel resampling as the most intuitive and simple one.

3.2.3. Skull stripping

Skull stripping is a method to localize the region of interest and filter out potential False Positives. To test how skull stripping affects model performance, we use HD-BET Isensee et al. [2019], which is the most accurate publicly available brain extraction tool. We extract brain mask on CT1 and apply it to all other MR modalities after image alignment (this results in no loss of tumor mask).

3.3. Models architecture and training

We test the effect of preprocessing on two deep-learning segmentation architectures: 3D nn-UNet Isensee et al. [2021] and vision transformer-based 3D UNETR Hatamizadeh et al. [2022].

In all experiments we trained networks for 300 epochs or until convergence (using 20 epochs patience as a stopping criterion) without data augmentations, as data augmentation can interfere with measurements of preprocessing effects. All experiments were performed on a 3-fold cross-validation (subject-wise) with the average time for one experiment being 20 hours on 32 GB Tesla V100.

3.4. Perfomance metrics

The accuracy of brain MRI semantic segmentation is conventionally evaluated using the Dice Similarity coefficient (referred to as Dice) and the 95th percentile of the Hausdorff distance between the predicted labels and the provided ground truth, these metrics are used for SOTA models evaluation on benchmark datasets. Bakas et al. [2022].

In the current work we focus on overlap-based metric Dice coefficient as the standard for assessing the quality of segmentation and provide clear and

meaningful interpretations:

$$\text{Dice } (A, B) = \frac{2 \cdot |A \cap B|}{|A| + |B|}, \tag{1}$$

where A and B are 3D binary arrays. In addition, to measure the error in terms of tumor volume estimation, which is the simplest clinically relevant feature Chang et al. [2019], we use Mean Absolute Error (MAE):

$$\text{MAE}(V_{\text{true}}, V_{\text{estimated}}) = \frac{1}{n} \sum_{i=1}^{n} |V_{\text{true}}^i - V_{\text{estimated}}^i|. \tag{2}$$

Mean and standard deviation for Dice score and absolute errors were obtained out of fold. We also asses absolute volumetric error of estimation (for evaluation of result significance from the clinical perspective).

To measure the differences in voxel intensity between healthy and tumored tissues for different image enhancement experiments, we use Kullback-Leibler divergence (KL) between corresponding intensity histograms:

$$\text{KL}(H_{\text{healthy}}, H_{\text{tumor}}) = \sum_{i=1}^{\#\text{bins}} H_{\text{healthy}}^i \cdot \log \frac{H_{\text{healthy}}^i}{H_{\text{tumor}}^i} \tag{3}$$

We report KL values for histograms with fixed bin size (100 bins), and we have tested the Freedman-Diaconis heuristic Freedman and Diaconis [1981] (500-700 bins depending on subject) and Sturge's rule Sturges [1926] (20-60 bins). All approaches result in different absolute KL values but preserve a relative trend, without affecting the experiment's conclusion.

To assess the results' significance and compare experiments with different data preprocessing, we test the Null hypothesis of the Means equality in two samples with Welch's t-test Bonferroni corrected for multiple comparisons. If the p_{value} for the test has not exceeded 0.05, we declare that there is no evidence in the data for rejecting the Null hypothesis. For simplicity, from now on we will refer to it as statistically significant.

3.5. Data description

We explore the effect of data preprocessing for tumor segmentation on multi-modal brain MRI data (a task similar to an extensively studied BraTS Menze et al. [2014]). We selected three largest publicly available multi-domain with original DICOM data from TCIA Clark et al. [2013a]: Glioblastoma Multi-form (GBM) and Lower Grade Glioma (LGG) Beers et al. [2018b]; Bakas et al. [2017b]; Beers et al. [2018a], and an in-house dataset of 180 patients with glioblastoma (BGPD)Zolotova et al. [2023].

All three datasets contain 4 MR sequences (T1, T2, CT1, FLAIR) available in a raw DICOM format, without any prior preprocessing. All three datasets comprise of multi-protocol studies (Table 3). A summary of all datasets is presented in Table 2. A more detailed description is given below.

Table 2: Description of open-source multi-institutional datasets on brain tumor segmentation used in the study. All datasets have multimodal MR set per patient, including: CT1, T1, T2 and FLAIR modalities.

Dataset	Dataset name	Size	Diagnosis	Preprocessing	Segmentation classes	Annotation source
Beers et al. [2018a]	LGG	38	pre-operative low-grade glioma	✗	WT, ET	semi-automatic
Beers et al. [2018a]	GBM	102	pre-operative glioblastoma	✗	WT, ET, TC	semi-automatic
Zolotova et al. [2023]	BGPD	180	pre-radiotherapy glioblastoma	✗	GTV	manual

3.5.1. Glioblastoma Multiforme (GBM) Dataset

GBM is an open-source data collection Bakas et al. [2017a,c]; Clark et al. [2013b]; Beers et al. [2018b] which originally included 262 patients with pre-processed images. We selected 102 patients with accessible segmentation labels for data without preprocessing[4]. The annotations are semi-automatic, obtained using a GLISTRBoost Bakas et al. [2015] tool with manual correction, and include segmentation for the whole tumor (WT), tumor core (TC) and enhancing tumor (ET). The data subset is comprised of data from 3 manufacturers and at least 28 different study protocols.

3.5.2. Low Grade Glioma (LGG) Dataset

LGG is an open-source data collection Pedano et al. [2016] that originally included 199 patients. We selected a subset of 38 unique patients with accessible segmentation labels for data without preprocessing. The annotations are semi-automatic, obtained using a GLISTRBoost Bakas et al. [2015] tool with manual correction, and include segmentation for WT and ET (38 out of the selected 39 images do not contain TC segmentation map and are thus excluded from the experiments for LGG). The ata subset is comprised of data from 3 manufacturers and at least 11 different study protocols.

3.5.3. Burdenko Glioblastomas Progression Dataset (BGPD)

BGPD Zolotova et al. [2023] is an MRI collection of patients who underwent radiotherapy in Burdenko Neurosurgery Institute for Radiotherapy in Moscow, Russia. It contains the data of 180 unique patients. Segmentation maps were imported from a radiotherapy planning system and correspond to Gross Tumor Volume (GTV). The collection is highly heterogeneous and comprised of data from 4 manufacturers and at least 51 different study protocols.

4. Results

Our results are four-fold. First, we analyze the effect of image resampling (Steps 2-4 Figure 1). Second, we analyze image enhancement methods (Steps 4.a-4.c Figure 1). Next, we discuss the utility of skull-stripping in terms of segmentation metrics and volume estimates. Finally, we analyze if there is optimal preprocessing in a transfer learning scenario. We end the results section

---

[4]https://wiki.cancerimagingarchive.net/pages/viewpage.action?pageId=41517733

Table 3: Variability of study protocols for T1 and T2 MRI sequences for GBM, BGPD and LGG data collections. All datasets contain images from 3 major MRI scanner manufacturers: GE, Siemens, and Toshiba.

Aquisition parameter		GBM		BGPD		LGG	
		T1	T2	T1	T2	T1	T2
Echo Time, ms	min	2.1	20	1.8	18.4	3.7	16.1
	max	19	120	23	120	15	120
	#unique	28	38	51	67	11	17
Repetition Time, ms	min	5	2020	7.4	567	8	897
	max	3379.6	6650	3119.2	8200	3232	10000
	#unique	56	36	50	57	38	18
Voxel volume, mm^3	min	0.5	0.2	0.1	0.1	0.6	0.5
	max	5.2	5.2	5.3	4.8	13.2	35.2
	#unique	32	32	53	60	17	19

Table 4: nnU-net and UNETR segmentation performance for the three datasets: GBM and LGG (WT label), BGPD (GTV label). Segmentation accuracy presented in Dice scores from three fold cross-validation as Mean (STD) multiplied by 100, the higher — the better. Models trained for 300 epochs. Arrows denote the statistically significant difference ($p_{\mathrm{value}} < 0.05$) compared to step 4. Resampling to spacing, $\uparrow$ (increase), $\downarrow$ (decrease).

	nnU-net			UNETR		
Data preprocessing	GBM	BGPD	LGG	GBM	BGPD	LGG
1. Inter-modality registration	44 (28) $\downarrow$	36 (29) $\downarrow$	67 (27)	39 (26) $\downarrow$	35 (30) $\downarrow$	66 (23)
2. Resampling to image size	85 (11)	73 (19)	72 (24)	82 (12)	67 (20)	66 (26)
3. Atlas registration	85 (11)	75 (16)	71 (25)	82 (13)	68 (21)	67 (25)
4. Resampling to spacing	85 (12)	74 (18)	70 (25)	83 (14)	67 (21)	67 (23)
4.a Bias field correction	82 (13) $\downarrow$	75 (17)	67 (25)	80 (13)	72 (19) $\uparrow$	62 (22)
4.b Denoising	84 (12)	74 (17)	70 (26)	83 (13)	69 (21) $\uparrow$	65 (25)
4.c Histogram matching	83 (16)	75 (16)	68 (26)	81 (16)	68 (18)	63 (26)
4.d Skull stripping	87 (11)	76 (14) $\uparrow$	77 (21) $\uparrow$	85 (11)	72 (18) $\uparrow$	75 (19) $\uparrow$

with our recommendations on MRI images preprocessing for deep learning-based tumor segmentation.

4.1. Inter-subject image alignment

Table 4 shows validation results of nnU-net and UNETR architectures for the three datasets.

First, for two larger datasets (GBM and BGPD) we observe that introducing some resampling strategy to homogenise voxel volume across the dataset is always beneficial, Table 4 step 1 versus steps 2-4. Recall that without any voxel resampling, the differences between voxels' volumes are as large as 10 times for GBM (0.5 mm^3 versus 5.2 mm^3), and 53 times for BGPD (0.1 mm^3 versus 5.3 mm^3), see Table 3. Thus, for a 3D convolutional neural network, the receptive field of a convolution filter will differ by a factor of 53. Interestingly,

while for the LGG dataset we also have a difference between voxels' spacing by a factor of 22, there are no significant differences in performance between steps 1-4. The latter might be the consequence of a relatively small sample size.

Second, we observe that applying non-rigid Atlas registration (step 3) lead to the same results compared to a faster Resampling to the same image size (step 2) or Resampling all images to the same voxel spacing (step 4). For both NN architectures in all datasets, it is not possible to reject the Null hypothesis about the equality of means ($p_{\text{values}} > 0.1$, accounting multiple comparisons correction). Recall that images on step 3 are both the same image size and have a voxel of the same volume[5].

4.2. Image enhancement

We compare three different intensity normalization steps commonly used in brain MRI analysis pipelines: Bias field correction (step 4.a), Denoising (step 4.b) and Histogram matching (step 4.c). As there were no significant differences found between resampling approaches, steps 4.a-c were performed after resampling images to the same voxel volume (step 4).

First, for a convolutional nnU-net, intensity correction transformations could be completely omitted. As show in Table 4, there is no statistically significant improvement of either of steps 4.a-c compared to step 4 ($p_{\text{values}} > 0.1$) for all three datasets. In most of the cases, the average segmentation performance is actually worse (compared to no intensity normalization, step 2) by an absolute value, though the only statistically significant drop in performance is Bias field correction on GBM dataset (82 mean Dice score (step 4.a) compared to 85 mean Dice score (step 4), $p_{\text{value}} = 0.014$).

Second, for an attention-based model, the general trend stays the same, except for the BGPD dataset and steps 4.a and b. Here, we observe a small but statistically significant increase in performance. We do not have a reasonable explanation for the effect (see Appendix A), though we acknowledge that for all datasets, UNETR architecture results in worse performance compared to nnU-net. This might be the effect of a relatively small sample size, as transformer-based architectures require more training data.

4.3. Skull stripping

A brain mask application before training results in a moderate but statistically significant Dice score improvement for BGPD and LGG datasets (both nnU-net and UNETR) over the experiment without skull stripping, see Table 4 4 and 4.d. For the GBM dataset, the average segmentation quality is larger and the standard deviation is smaller in the experiment with skull stripping, though after a multiple comparisons correction these differences are not statistically significant ($p_{\text{value}} = 0.09$).

---

[5]Resampling to same image size results in almost equal voxel volumes 1.07 (0.34) mm^3, mean (std) for BGPD dataset.

Table 5: Estimated MAE of model prediction from ground truth label for the three datasets: GBM and LGG (WT label), BGPD (GTV label). Results are represented in mL, values are Mean (STD), the lower — the better. Volumes estimates are based on nnU-net. Arrows denote statistically significant difference ($p_{\text{value}} < 0.05$) compared to step 4. Resampling to spacing ↑ (increase), ↓ (decrease).

Data preprocessing	GBM	BGPD	LGG
1.Inter-modality registration	63 (47) ↓	55 (62) ↓	34 (39)
2.Resampling to image size	15 (14)	28 (43)	23 (24)
3.Atlas registration	13 (11)	27 (45)	31 (33)
4.Resampling to spacing	14 (13)	28 (49)	32 (31)
4.a Bias field correction	15 (15)	27 (49)	34 (37)
4.b Denoising	13 (13)	27 (47)	32 (34)
4.c Histogram matching	14 (12)	27 (47)	42 (61)
4.d Skull stripping	10 (9) ↑	26 (42)	19 (17) ↑

4.4. Volumetric errors

In addition to the Dice scores, we provide the errors in tumour volume estimates for different preprocessing steps.

We report the results for nnU-net in Table 5, as it performs better in our experiments. In terms of volume estimates, errors follow the same trend as with Dice scores: inter-subject alignment is always beneficial, image enhancement does not result in any improvements, and skull stripping systematically improves the quality.

In volume estimates, skull stripping improves tumor segmentation quality for GBM and LGG datasets (step 4.d., Table 5) and does not for the BGPD dataset (for which there is a statistically significant improvement in terms of Dice scores). This result itself is aligned with the results in Dice scores, yet it is an argument for using clinically relevant metrics in addition to segmentation metrics.

Volumetric errors of model predictions on BGPD data with and without skull stripping are not statistically significant (MAE 26 (42) mL for skull stripping and MAE 28 (49) mL without skull stripping, $p_{\text{value}} = 0.308$), thus from a clinical perspective this additional step is not completely justified. Complete volumetric measurements for all experiments are provided in the Appendix A. Additionally, we check if error in volume estimate depends on tumor total size (Figure 3), and do not observe any dependence.

4.5. Transfer learning.

We test if MRI data preprocessing can facilitate model transfer from another dataset. In particular, we explore if model fine-tuning after training on preprocessed data is better than model fine-tuning on non-preprocessed data.

We repeat the main ablation study with nnU-net models pretrained on the GBM dataset for 300 epochs and fine-tune them on BGPD with the same data
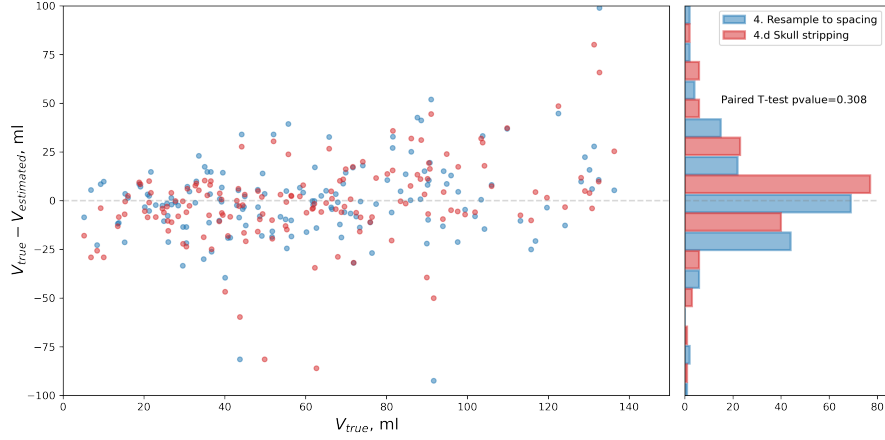
Figure 3: The relation between tumor volume and its' estimated volume from predicted segmentation mask for two nnU-net experiments on BGPD: 4. Resample to spacing and 4.d Resample to spacing with skull stripping.

(a) GBM dataset, WT label
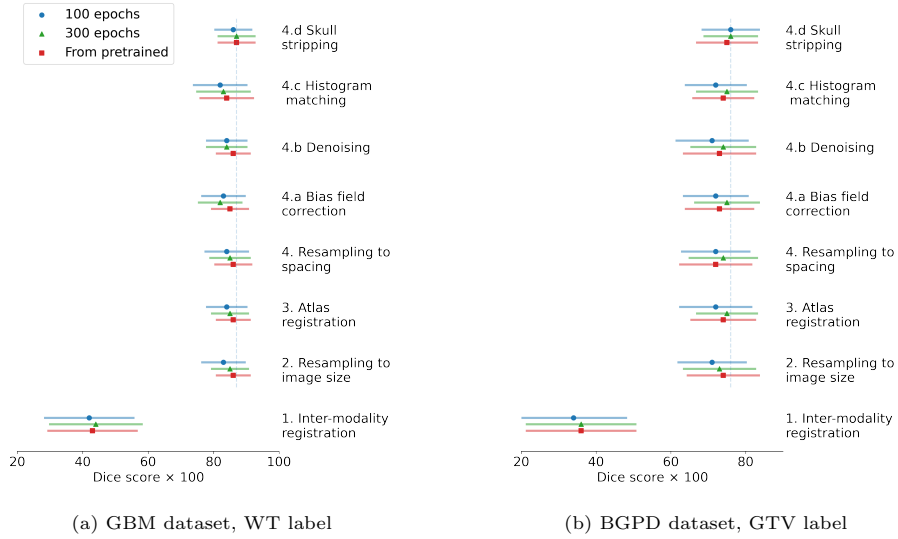
(b) BGPD dataset, GTV label

Figure 4: nnU-net performance on GBM and BGPD datasets. Horizontal: segmentation accuracy presented in Dice scores from three fold cross-validation as Mean (STD) multiplied by 100. Vertical: preprocessing experiments 1-4.d for models trained with random weights initialization for 100 epochs (blue), 300 epochs (green) and fine-tuning for 100 epochs from pretrained weighs on another dataset (red).

preprocessing for 100 epochs (and pretraining on BGPD with fine-tuning of GBM for corresponding experiments). We compare the Dice scores on three fold cross-validation for a model trained for 100 and 300 epochs from random weight initialization, and a model trained on 100 epochs from pretrained weights. The results are presented in Figure 4.

First, we observe a definitive improvement in nnU-net performance on the GBM dataset with weight transfer and fine tuning for 100 epochs (red bars), compared to a training from scratch for 300 epochs (green bars), Figure 4a. For the BGPD dataset, pretraining on the GBM sample results in better segmentation performance compared to training for 100 epochs (blue bars and red bars), but worse compared to training from scratch for 300 epochs (green bars), Figure 4b. This effect could be a consequence of the different sample sizes, as BGPD is almost two times larger than GBM — thus pretraining on the BGPD improves GBM segmentation, but not vice versa.

Second, we do not observe any differences in segmentation performance for either of the preprocessing steps on both datsets. For example, for the GBM dataset and preprocessing step 4.b Denoising, a model trained for 100 epochs results in 84 (12) Dice score (STD), the same if trained for 300 epochs, and 86 (10) Dice score if fine-tuned from BGPD. Yet, with the same data preprocessing on BGPD, we see a decrease in the mean Dice score with weight transfer from the GBM dataset to BGPD. Similarly, for step 4.d, the improvement of the segmentation quality on the GBM dataset is not observable in the BGPD sample. From these experiments we conclude that no preprocessing step among those studied improves model performance with weight transfer for both datasets. Numerical results depicted in Figure 4 are accessible in Appendix C.

Lastly, we perform an experiment with model fine-tuning from two large datasets BraTS2021, consisting of 2000 subjects Baid et al. [2021] and EGD dataset with 774 subjects.van der Voort et al. [2021], with multiclass labels, similar to GBM and LGG ones. According to our results, model fine-tuning from a larger sample — the most exploited method of transfer learning Ardalan and Subbian [2022] — can be reached by longer training, irrespective of the size of the dataset for weight transfer, see Appendix B Table C.11.

4.6. Our recommendations for brain MRI preprocessing for deep learning segmentation.

The overall results suggest the following recommendations:

- It's essential to align multi-modal MRI data between subjects for analysis, and even fast methods like image or voxel resizing yield comparable to atlas registration segmentation accuracy.

- Bias-field correction, denoising, and histogram matching are unnecessary in MRI segmentation pipelines based on UNet-like or UNETR architectures.

- Although skull stripping can improve segmentation performance, its impact on clinical measurements, such as differences in lesion volume esti-

mates, is relatively small. Therefore, depending on the clinical task and the need for fast processing times, this step may not be necessary.

- Preprocessing MRI data does not help with transfer learning while fine-tuning models on other datasets. Moreover, there's almost no significant difference between fine-tuning models from other data and just doing longer training on the original sample.

5. Conclusion

We perform a rigorous ablation study of the most conventional preprocessing steps used in the analysis of brain MRI images, including atlas registration, voxel resampling and image resizing, histogram matching, bias-field correction, denoising and skull stripping.

Although the image reprocessing steps might be useful for annotators and make distinct properties of the image more recognizable for the human eye, we show that only image alignment and voxel resampling are essential for accurate prediction with DNN models. We conclude that predictions after atlas registration do not significantly differ from ones with equal voxel resampling. We observe that bias-field correction, denoising, and histogram matching reduce data variance and do not affect DNN performance positively. We point out that skull stripping can lead to a measurable increase in accuracy and facilitate model convergence. On the other hand, brain extraction is very computationally expensive, and its incorporation into a pipeline does not affect clinically relevant volumetric measurements.

Thus we believe that skipping all steps excluding image alignment and voxel resampling from the brain MRI deep learning pipeline may reduce computational costs and improve reproducibility across studies.

These recommendations will be especially relevant for MRI data preprocessing for semi-automated labeling with Segment Anything Model (SAM) and modifications Kirillov et al. [2023]. SAM is a vision-transformer based architecture, shown to be extremely useful for data annotation, yet still not surpassing the SOTA solutions for brain MRI data segmentation Wu et al. [2023]. In the current work we define necessary preprocessing steps needed for MRI data annotation and further training, that will ensure reproducible across the studies and best segmentation accuracy.

5.1. Work limitations

Our findings on data preprocessing strategies suggest that overall research reproducibility will benefit if one discards custom preprocessing steps, including different skull stripping, various implementations of bias field correction, denoising, etc. Yet we observed that the results of transfer learning and model training from scratch are strictly related to datasets' homogeneity and size. These effects could be different on datests of thousands of images de Raad et al. [2021].

In the current study we focused on conventional brain MRI data preparation methods. The newly-developed methods of MRI harmonization, as multi

site image harmonization by cumulative distribution function (CDF) alignment (MICA Wrobel et al. [2020]) or robust intensity distribution alignment (RIDA) Sederevicius et al. [2022] could be outperforming the most conventional algorithms for histogram matching Nyúl et al. [2000]. Advanced image intensity enhancement methods can be compared with the explored ones, i.e. with orthogonal moments da Silva et al. [2022] for MR image enhancement. These analyses were outside the scope of the original study.

5.2. Authors contributions

Conceptualization and methodology, A.K., E.K. and P.D.; data pipeline organization and preprocessing pipeline E.K.; model training and analysis P.D.; interpretation of results, A.K. and A.D., S.Z., A.G.; writing original draft A.K., E.K. and P.D.; writing—review and editing, M.B., B.S. and A.D. All authors have read and agreed to the published version of the manuscript.

5.3. Declaration of Competing Interest

The authors declare that they have no known competing financial interests or personal relationships that could have appeared to influence the work reported in this paper.

5.4. Acknowledgments

References

Ardalan, Z., Subbian, V., 2022. Transfer learning approaches for neuroimaging analysis: A scoping review. Frontiers in Artificial Intelligence 5.

Avants, B.B., Tustison, N., Song, G., et al., 2009. Advanced normalization tools (ants). Insight j 2, 1–35.

Baid, U., Ghodasara, S., Mohan, S., Bilello, M., Calabrese, E., Colak, E., Farahani, K., Kalpathy-Cramer, J., Kitamura, F.C., Pati, S., et al., 2021. The rsna-asnr-miccai brats 2021 benchmark on brain tumor segmentation and radiogenomic classification. arXiv preprint arXiv:2107.02314 .

Bakas, S., Akbari, H., Sotiras, A., Bilello, M., Rozycki, M., Kirby, J., Freymann, J., Farahani, K., Davatzikos, C., 2017a. Segmentation labels and radiomic features for the pre-operative scans of the tcga-lgg collection. The cancer imaging archive 286.

Bakas, S., Akbari, H., Sotiras, A., Bilello, M., Rozycki, M., Kirby, J.S., Antony, J.B.A., Farahani, K., Davatzikos, C., 2017b. Advancing the cancer genome atlas glioma MRI collections with expert segmentation labels and radiomic features. Scientific Data 4. URL: https://doi.org/10.1038/sdata.2017.117, doi:10.1038/sdata.2017.117.

Bakas, S., Akbari, H., Sotiras, A., Bilello, M., Rozycki, M., Kirby, J.S., Freymann, J.B., Farahani, K., Davatzikos, C., 2017c. Advancing the cancer genome atlas glioma mri collections with expert segmentation labels and radiomic features. Scientific data 4, 1–13.

Bakas, S., Reyes, M., Jakab, A., Bauer, S., Rempfler, M., Crimi, A., Shinohara, R.T., Berger, C., Ha, S.M., Rozycki, M., et al., 2018. Identifying the best machine learning algorithms for brain tumor segmentation, progression assessment, and overall survival prediction in the brats challenge. arXiv preprint arXiv:1811.02629 .

Bakas, S., Sako, C., Akbari, H., Bilello, M., Sotiras, A., Shukla, G., Rudie, J.D., Santamaría, N.F., Kazerooni, A.F., Pati, S., et al., 2022. The university of pennsylvania glioblastoma (upenn-gbm) cohort: advanced mri, clinical, genomics, & radiomics. Scientific Data 9, 1–12.

Bakas, S., Zeng, K., Sotiras, A., Rathore, S., Akbari, H., Gaonkar, B., Rozycki, M., Pati, S., Davatzikos, C., 2015. Glistrboost: combining multimodal mri segmentation, registration, and biophysical tumor growth modeling with gradient boosting machines for glioma segmentation, in: BrainLes 2015, Springer. pp. 144–155.

Beare, R., Lowekamp, B., Yaniv, Z., 2018. Image segmentation, registration and characterization in r with simpleitk. Journal of statistical software 86.

Beers, A., Gerstner, E., Rosen, B., Clunie, D., Pieper, S., Fedorov, A., Kalpathy-Cramer, J., 2018a. Dicom-seg conversions for tcga-lgg and tcga-gbm segmentation datasets. [Data set]. The Cancer Imaging Archive. doi:10.7937/TCIA.2018.ow6ce3ml.

Beers, A., Gerstner, E., Rosen, B., et al., 2018b. Dicom-seg conversions for tcga-lgg and tcga-gbm segmentation datasets. Cancer Imaging Arch .

Berisha, V., Krantsevich, C., Hahn, P.R., Hahn, S., Dasarathy, G., Turaga, P., Liss, J., 2021. Digital medicine and the curse of dimensionality. NPJ digital medicine 4, 1–8.

Chang, K., Beers, A.L., Bai, H.X., Brown, J.M., Ly, K.I., Li, X., Senders, J.T., Kavouridis, V.K., Boaro, A., Su, C., et al., 2019. Automatic assessment of glioma burden: a deep learning algorithm for fully automated volumetric and bidimensional measurement. Neuro-oncology 21, 1412–1422.

Clark, K., Vendt, B., Smith, K., Freymann, J., Kirby, J., Koppel, P., Moore, S., Maffitt, D., Pringle, M., Tarbox, L., Prior, F., 2013a. The cancer imaging archive (TCIA): Maintaining and operating a public information repository. Journal of Digital Imaging 26, 1045–1057. URL: https://doi.org/10.1007/s10278-013-9622-7, doi:10.1007/s10278-013-9622-7.

Clark, K., Vendt, B., Smith, K., Freymann, J., Kirby, J., Koppel, P., Moore, S., Phillips, S., Maffitt, D., Pringle, M., et al., 2013b. The cancer imaging archive (tcia): maintaining and operating a public information repository. Journal of digital imaging 26, 1045–1057.

Dai, C., Mo, Y., Angelini, E., Guo, Y., Bai, W., 2019. Transfer learning from partial annotations for whole brain segmentation, in: Domain Adaptation and Representation Transfer and Medical Image Learning with Less Labels and Imperfect Data. Springer, pp. 199–206.

Eijgelaar, R.S., Visser, M., Müller, D.M., Barkhof, F., Vrenken, H., van Herk, M., Bello, L., Conti Nibali, M., Rossi, M., Sciortino, T., et al., 2020. Robust deep learning–based segmentation of glioblastoma on routine clinical mri scans using sparsified training. Radiology: Artificial Intelligence 2, e190103.

Ermiş, E., Jungo, A., Poel, R., Blatti-Moreno, M., Meier, R., Knecht, U., Aebersold, D.M., Fix, M.K., Manser, P., Reyes, M., et al., 2020. Fully automated brain resection cavity delineation for radiation target volume definition in glioblastoma patients using deep learning. Radiation oncology 15, 1–10.

Freedman, D., Diaconis, P., 1981. On the histogram as a density estimator: L 2 theory. Zeitschrift für Wahrscheinlichkeitstheorie und verwandte Gebiete 57, 453–476.

Győrfi, Á., Szilágyi, L., Kovács, L., 2021. A fully automatic procedure for brain tumor segmentation from multi-spectral mri records using ensemble learning and atlas-based data enhancement. Applied Sciences 11, 564.

Hatamizadeh, A., Yang, D., Roth, H.R., Xu, D., 2022. Unetr: Transformers for 3d medical image segmentation. 2022 IEEE/CVF Winter Conference on Applications of Computer Vision (WACV) , 1748–1758.

Isensee, F., Jaeger, P.F., Kohl, S.A., Petersen, J., Maier-Hein, K.H., 2021. nnu-net: a self-configuring method for deep learning-based biomedical image segmentation. Nature methods 18, 203–211.

Isensee, F., Schell, M., Pflueger, I., Brugnara, G., Bonekamp, D., Neuberger, U., Wick, A., Schlemmer, H.P., Heiland, S., Wick, W., et al., 2019. Automated brain extraction of multisequence mri using artificial neural networks. Human brain mapping 40, 4952–4964.

Juntu, J., Sijbers, J., Van Dyck, D., Gielen, J., 2005. Bias field correction for mri images, in: Computer recognition systems. Springer, pp. 543–551.

Kickingereder, P., Isensee, F., Tursunova, I., Petersen, J., Neuberger, U., Bonekamp, D., Brugnara, G., Schell, M., Kessler, T., Foltyn, M., et al., 2019. Automated quantitative tumour response assessment of mri in neuro-oncology with artificial neural networks: a multicentre, retrospective study. The Lancet Oncology 20, 728–740.

Kirillov, A., Mintun, E., Ravi, N., Mao, H., Rolland, C., Gustafson, L., Xiao, T., Whitehead, S., Berg, A.C., Lo, W.Y., Dollár, P., Girshick, R., 2023. Segment anything. arXiv:2304.02643 .

Kondrateva, E., Pominova, M., Popova, E., Sharaev, M., Bernstein, A., Burnaev, E., 2021. Domain shift in computer vision models for mri data analysis: an overview, in: Thirteenth International Conference on Machine Vision, International Society for Optics and Photonics. p. 116050H.

Kurmukov, A., Dalechina, A., Saparov, T., Belyaev, M., Zolotova, S., Golanov, A., Nikolaeva, A., 2021. Challenges in building of deep learning models for glioblastoma segmentation: Evidence from clinical data., in: MIE, pp. 298–302.

Li, Y., Ammari, S., Balleyguier, C., Lassau, N., Chouzenoux, E., 2021. Impact of preprocessing and harmonization methods on the removal of scanner effects in brain mri radiomic features. Cancers 13, 3000.

Menze, B., Isensee, F., Wiest, R., Wiestler, B., Maier-Hein, K., Reyes, M., Bakas, S., 2021. Analyzing magnetic resonance imaging data from glioma patients using deep learning. Computerized medical imaging and graphics 88, 101828.

Menze, B.H., Jakab, A., Bauer, S., Kalpathy-Cramer, J., Farahani, K., Kirby, J., Burren, Y., Porz, N., Slotboom, J., Wiest, R., et al., 2014. The multimodal brain tumor image segmentation benchmark (brats). IEEE transactions on medical imaging 34, 1993–2024.

Moradmand, H., Aghamiri, S.M.R., Ghaderi, R., 2020. Impact of image preprocessing methods on reproducibility of radiomic features in multimodal magnetic resonance imaging in glioblastoma. Journal of applied clinical medical physics 21, 179–190.

Nixon, M., Aguado, A., 2019. Feature extraction and image processing for computer vision. Academic press.

Nyúl, L.G., Udupa, J.K., Zhang, X., 2000. New variants of a method of mri scale standardization. IEEE transactions on medical imaging 19, 143–150.

Patro, S., Sahu, K.K., 2015. Normalization: A preprocessing stage. arXiv preprint arXiv:1503.06462 .

Pedano, N., Flanders, A., Scarpace, L., Mikkelsen, T., Eschbacher, J., et al., 2016. Cancer genome atlas low grade glioma (tcga-lgg) data collection. Cancer Imaging Archive .

Pei, L., Bakas, S., Vossough, A., Reza, S.M., Davatzikos, C., Iftekharuddin, K.M., 2020. Longitudinal brain tumor segmentation prediction in mri using feature and label fusion. Biomedical signal processing and control 55, 101648.

Pérez-García, F., Sparks, R., Ourselin, S., 2021. Torchio: a python library for efficient loading, preprocessing, augmentation and patch-based sampling of medical images in deep learning. Computer Methods and Programs in Biomedicine , 106236URL: https://www.sciencedirect.com/science/article/pii/S0169260721003102, doi:https://doi.org/10.1016/j.cmpb.2021.106236.

de Raad, K., van Garderen, K., Smits, M., van der Voort, S., Incekara, F., Oei, E., Hirvasniemi, J., Klein, S., Starmans, M., 2021. The effect of preprocessing on convolutional neural networks for medical image segmentation, in: 2021 IEEE 18th International Symposium on Biomedical Imaging (ISBI), IEEE. pp. 655–658.

Ranjbarzadeh, R., Bagherian Kasgari, A., Jafarzadeh Ghoushchi, S., Anari, S., Naseri, M., Bendechache, M., 2021. Brain tumor segmentation based on deep learning and an attention mechanism using mri multi-modalities brain images. Scientific Reports 11, 1–17.

Rathore, S., Bakas, S., Pati, S., Akbari, H., Kalarot, R., Sridharan, P., Rozycki, M., Bergman, M., Tunc, B., Verma, R., et al., 2017. Brain cancer imaging phenomics toolkit (brain-captk): an interactive platform for quantitative analysis of glioblastoma, in: International MICCAI Brainlesion Workshop, Springer. pp. 133–145.

Rohlfing, T., Zahr, N.M., Sullivan, E.V., Pfefferbaum, A., 2010. The sri24 multichannel atlas of normal adult human brain structure. Human brain mapping 31, 798–819.

Sederevicius, D., Bjornerud, A., Walhovd, K.B., Van Leemput, K., Fischl, B., Fjell, A.M., 2022. A robust intensity distribution alignment for harmonization of t1w intensity values. bioRxiv .

da Silva, R.D.C., Jenkyn, T.R., Carranza, V.A., 2022. Enhanced pre-processing for deep learning in mri whole brain segmentation using orthogonal moments. Brain Multiphysics 3, 100049.

Smith, S.M., Brady, J.M., 1997. Susan—a new approach to low level image processing. International journal of computer vision 23, 45–78.

Sturges, H.A., 1926. The choice of a class interval. Journal of the american statistical association 21, 65–66.

Thakur, S., Doshi, J., Pati, S., Rathore, S., Sako, C., Bilello, M., Ha, S.M., Shukla, G., Flanders, A., Kotrotsou, A., et al., 2020. Brain extraction on mri scans in presence of diffuse glioma: Multi-institutional performance evaluation of deep learning methods and robust modality-agnostic training. Neuroimage 220, 117081.

Tustison, N.J., Avants, B.B., Cook, P.A., Zheng, Y., Egan, A., Yushkevich, P.A., Gee, J.C., 2010. N4itk: improved n3 bias correction. IEEE transactions on medical imaging 29, 1310–1320.

van der Voort, S.R., Incekara, F., Wijnenga, M.M., Kapsas, G., Gahrmann, R., Schouten, J.W., Dubbink, H.J., Vincent, A.J., van den Bent, M.J., French, P.J., et al., 2021. The erasmus glioma database (egd): Structural mri scans, who 2016 subtypes, and segmentations of 774 patients with glioma. Data in brief 37, 107191.

Wang, G., Shapey, J., Li, W., Dorent, R., Dimitriadis, A., Bisdas, S., Paddick, I., Bradford, R., Zhang, S., Ourselin, S., et al., 2019. Automatic segmentation of vestibular schwannoma from t2-weighted mri by deep spatial attention with hardness-weighted loss, in: International Conference on Medical Image Computing and Computer-Assisted Intervention, Springer. pp. 264–272.

Wang, X., Li, X.H., Cho, J.W., Russ, B.E., Rajamani, N., Omelchenko, A., Ai, L., Korchmaros, A., Sawiak, S., Benn, R.A., et al., 2021. U-net model for brain extraction: Trained on humans for transfer to non-human primates. Neuroimage 235, 118001.

Wightman, R., Touvron, H., Jégou, H., 2021. Resnet strikes back: An improved training procedure in timm. arXiv preprint arXiv:2110.00476 .

Wrobel, J., Martin, M., Bakshi, R., Calabresi, P.A., Elliot, M., Roalf, D., Gur, R.C., Gur, R.E., Henry, R.G., Nair, G., et al., 2020. Intensity warping for multisite mri harmonization. NeuroImage 223, 117242.

Wu, J., Fu, R., Fang, H., Liu, Y., Wang, Z., Xu, Y., Jin, Y., Arbel, T., 2023. Medical sam adapter: Adapting segment anything model for medical image segmentation. arXiv preprint arXiv:2304.12620 .

Zolotova, S.V., Golanov, A.V., Pronin, I.N., Dalechina, A.V., Nikolaeva, A.A., Belyashova, A.S., Usachev, D.Y., Kondrateva, E.A., Druzhinina, P.V., Shirokikh, B.N., Saparov, T.N., Belyaev, M.G., Kurmukov, A.I., 2023. Burdenko's glioblastoma progression dataset (burdenko-gbm-progression) (version 1) [data set]. URL: https://doi.org/10.7937/E1QP-D183, doi:10.7937/E1QP-D183.

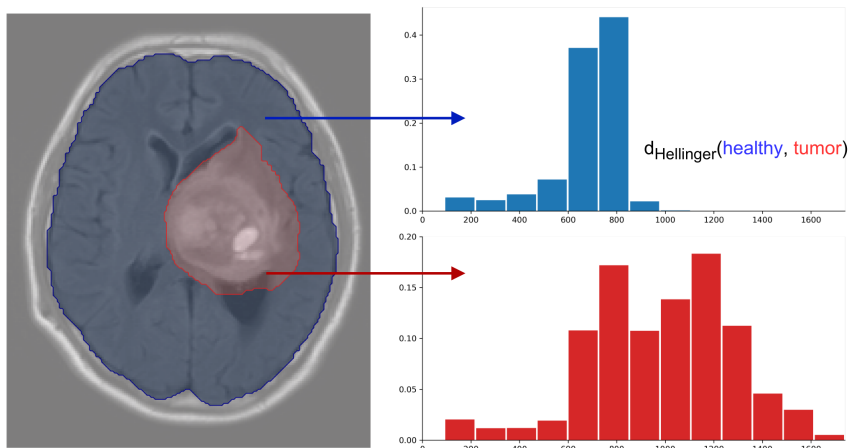## Appendix A. The effect of image enhancement

Figure A.5: Computing the distance between healthy tissue and tumor tissue regions.

Why do image enhancement methods not facilitate segmentation?

We attempt to explain why popular intensity normalization steps have questionable effect on segmentation performance. Our hypothesis is that while these steps equalize modalities appearance across the data, they also reduce the differences between voxels' intensities within each individual image. We compare intensity distribution for healthy brain voxels and voxels inside a tumor mask using Kullback-Leibler divergence (Table A.6). We expect that if preprocessing steps increases KL divergence it should result in increased segmentation quality, and vice versa. In most of the cases this supposition holds. Two exceptions are Denoising for Tumor core segmentation and Histogram matching for Enhancing tumor segmentation.

We report KL values for histograms with fixed bin size (30 bins), and we test the Freedman-Diaconis heuristic (500-700 bins depending on subject) and Sturge's rule (20-60 bins). Both approaches result in different absolute KL values but preserve a relative trend, without affecting the experiment conclusion.

In most cases, if the KL divergence decreases (differences between healthy and tumor tissue decrease), model performance decreases, too, and vice versa (steps 4.a-d in comparison to step 4, Table A.6). In almost all cases, lower KL values corresponds to lower performance, e.g. for bias-field correction, the KL between healthy brain and WT tissue is equal to 0.47, compared to 0.61 of atlas registration, which coincides with a segmentation quality drop (from 86.4 for atlas registration to 84.9 for bias-field corrected data). On the contrary, for denoised data, the KL are either the same or slightly larger compared to atlas data: 0.63 vs 0.61 for WT; 4.16 vs 4.01 for TC and 7.11 vs 6.70 for ET, which completely coincides with segmentation performance. The only comparison that

does not follow this explanation is bf-correction for TC (it has a lower KL compared to atlas data, but slightly better segmentation quality).

Table A.6: KL divergence values (KL) and JS distance (JS) between intensity histograms for masked brain w/o tumor and tumor region. Lower values correspond to smaller differences in voxel intensities between healthy (brain mask without Whole Tumor(WT) for GBM and RT for BGPD sample) and tumor tissue. Stars represent statistically significant difference to 4. Resampling to spacing distances.

Data preprocessing	GBM, KL	GBM, JS	BGPD, KL	BGPD, JS
4. Resampling to spacing	0.830(0.450)	0.303(0.095)	1.640(1.015)	0.477(0.129)
4.a Bias-field correction	0.660(0.300)	0.259(0.087)	1.145(0.723)	0.465(0.120)
4.b Denoising	0.870(0.470)	0.308(0.097)	1.702(1.045)	0.484(0.129)
4.c Histogram matching	0.770(0.470)	0.304(0.095)	1.650(1.029)	0.478(0.130)

Appendix B. Model architectures and training

nnU-net. We use NVIDIA's nn-Unet implementation for the BraTS2021 challenge[6]. The following changes were applied by the authors on top of the default nnU-net architecture Isensee et al. [2021]: increasing the encoder depth to 7, modifying the number of convolution channels to $[64, 96, 128, 192, 256, 384, 512]$, and using deep supervision — two additional output heads at the decoder levels. The model has multi-modal input of four modalities [T1, CT1, T2, FLAIR], plus a channel with one-hot encoding for foreground voxels, generated by image thresholding. We train nn-Unet with a patch size of `[128,128,128]` voxels and a batch size of two, a learning rate of 0.0003 and a `Adam` optimizer with `momentum` of 0.99.

UNETR. We use vision a transformer-based model UNETR Hatamizadeh et al. [2022] with an embedding size of 512 for a 1D sequence of a 3D input of the same 5 channels with patches of `[128,128,128]` voxels and the resolution of each patch equals 16. The model has 10 heads and is trained with learning rate

---

[6]github.com/NVIDIA/DeepLearningExamples/tree/ddbcd54056e8d1bc1c4d5a8ab34cb570ebea1947/PyTorch/Segmentation/nnUNet

Table B.7: Hyperparameters for nnU-net and UNETR models.

Parameter name	nnU-net	UNETR
learning rate	0.0003	0.0001
weight decay	0	0.00001
momentum	0.99	0.99
patch size	$[128, 128, 128]$	$[128, 128, 128]$
batch size	2	2

0.0001, with a `weight decay` of 0.00001, and an `Adam` optimizer with `momentum` of 0.99.

Model optimization. For the BGPD dataset we train the model to predict one class label. For the GBM dataset we train the model on three classes, according to the BraTS data labelling: WT, ET, TC. The model is then trained with the complex loss function. Each label class is optimized separately with the weighted sum of binary Cross-Entropy and the Dice loss (the trade-off weight value to 1 for both losses). The final complex loss function is optimized for a combination of class labels: the whole tumor (WT) (describes the union of the tumor core (ET), the non-enhancing part of the tumor core (NET) and the peritumoral edema ED), the tumor core (TC) (the union of the ET and NET), and the ET.
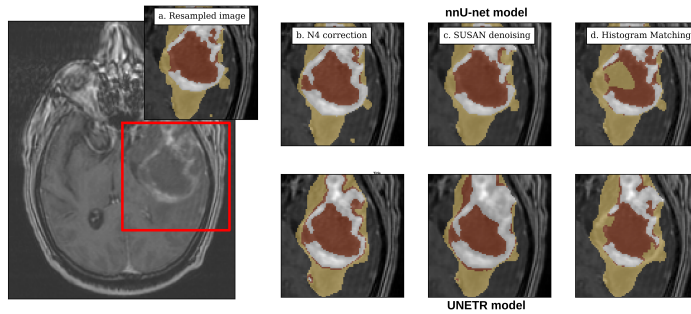

Figure B.6: Visualization of the two models' predictions with respect to the method of image intensity correction. The top raw (b-d) showing the image segmentation on 3 classes with nnUnet model (a) an example CT1 MR image from GBM data after resampling to [1,1,1] voxel size; (b) N4 correction of the image; (c) SUSAN denoising of the image; (d) Histogram standartization; The bottom row showing tumor segmentation with UNETR model. Colors: ET - red, TC - white, WT - yellow.

Appendix C. Additional illustration of the results

In this section we show additional illustrations of the results not represented in the test's main body. In Tables C.8 and C.9 we show the results of other segmentation classes for multiclass tumor segmentation mask (WT, ET and TC) for the GBM dataset and (WT and ET) for the LGG dataset.

In Table C.10 we show the numerical representation of graphical results from Figure 4.

Table C.8: nnU-net and UNETR segmentation performance for three-class (Whole tumor, Enhancing tumor, Tumor core) segmentation on GBM dataset. Numbers are Dice scores mean (std) multiplied by 100. Trained for 300 epoch, columns 1 and 4 are duplicated from Table 4.

	nnU-net			UNETR		
Data preprocessing	WT	ET	TC	WT	ET	TC
1. Inter-modality registration	44 (28) ↓	37 (30) ↓	30 (27) ↓	39 (26) ↓	32 (26) ↓	28 (24) ↓
2. Resampling to image size	85 (11)	80 (18)	74 (19)	82 (12)	75 (18)	72 (19)
3. Atlas registration	85 (11)	80 (17)	72 (20)	82 (13)	74 (18)	69 (21)
4. Resampling to spacing	85 (12)	80 (16)	73 (19)	83 (14)	75 (20)	71 (22)
4.a Bias field correction	82 (13) ↓	80 (17)	72 (19)	80 (13)	75 (20)	71 (21)
4.b Denoising	84 (12)	80 (17)	73 (20)	83 (13)	75 (20)	70 (22)
4.c Histogram matching	83 (16)	78 (20)	72 (21)	81 (16)	72 (24)	68 (24)
4.d Skull stripping	87 (11)	82 (16)	76 (19)	85 (11)	79 (16)	75 (19)

Table C.9: nnU-net and UNETR segmentation performance for two-classes (Whole tumor, Enhancing tumor) segmentation on LGG dataset. Numbers are Dice scores mean(std) multiplied by 100, columns 1 and 3 are duplicated from Table 4.

	nnU-net		UNETR	
Data preprocessing	WT	ET	WT	ET
1. Inter-modality registration	67 (27) ↓	47 (29)	66 (23)	49 (26)
2. Resampling to image size	72 (24)	52 (27)	66 (26)	49 (27)
3. Atlas registration	71 (25)	52 (29)	67 (25)	49 (27)
4. Resampling to spacing	70 (25)	48 (28)	67 (23)	50 (25)
4.a Bias field correction	67 (25)	45 (29)	62 (22)	45 (25)
4.b Denoising	70 (26)	51 (30)	65 (25)	48 (27)
4.c Histogram matching	68 (26)	49 (29)	63 (26)	45 (28)
4.d Skull stripping	77 (21) ↑	54 (25) ↑	75 (19) ↑	54 (25) ↑

Table C.10: nnU-net performance on GBM and BGPD datasets, numerical representation of Figure 4. Segmentation accuracy presented in Dice scores from three fold cross-validation as Mean (STD) multiplied by 100. Models trained with random weights initialization for 100 epochs, 300 epochs and fine-tuning for 100 epochs from pretrained weighs on other dataset (BGPD-GBM, GBM-BGPD finetune). Columns 2 and 5 are duplicated from Table 4.

	GBM			BGPD		
Data preprocessing	100 epochs	300 epochs	BGPD-GBM	100 epochs	300 epochs	GBM-BGPD
1. Inter-modality registration	42 (27)	44 (28)	43 (27)	34 (28)	36 (29)	36 (29)
2. Resampling to image size	83 (13)	85 (10)	86 (10)	71 (18)	73 (19)	74 (19)
3. Atlas registration	84 (12)	85 (11)	86 (10) ↑	72 (19)	75 (16)	72 (17)
4. Resampling to spacing	84 (13)	85 (12)	86 (11)	72 (18)	74 (18)	72 (19)
4.a Bias field correction	83 (13)	82 (13)	85 (11) ↑	72 (17)	75 (17)	73 (18)
4.b Denoising	84 (12)	84 (12)	86 (10) ↑	71 (19)	74 (17)	73 (19)
4.c Histogram matching	82 (16)	83 (16)	84 (26)	72 (16)	75 (16)	74 (16)
4.d Skull stripping	86 (11)	87 (11)	87 (11)	76 (15)	76 (14)	75 (16)

Table C.11: nnU-net performance with and w/o model transfer from large datasets (BraTS2021 Baid et al. [2021] and EGD van der Voort et al. [2021]. Segmentation accuracy presented in Dice scores from three fold cross-validation as Mean (STD) multiplied by 100. Models were trained for 300 epochs and fine-tuned for 100 epochs from pretrained weights on the larger dataset (BraTS-BGPD, EGD-GBM, BraTS-EGD finetune). Columns 1 and 3 are duplicated from Table 4.

Data preprocessing	BGPD, 300 epochs	BraTS-BGPD, Finetune	GBM, 300 epochs	EGD-GBM, Finetune	EGD, 300 epochs	BraTS-EGD, Finetune
3. Atlas registration	75 (17)	74 (20)	85 (12)	84 (11)	–	–
4.d Skull stripping	76 (14)	75 (17)	87 (11)	86 (10)	83 (12)	83 (12)